Expanded View Figures

Figure EV1. Interactions between cristae-shaping proteins, lipid saturation, and mitochondrial phenotypes.

A Representative Airyscan confocal micrographs of yeast expressing matrix-localized RFP (mts-RFP). Scale bars, 2 μm.

B (Left) Frequency of mitochondrial abnormalities as assayed by analysis of mts-RFP. $N > 50$ cells were counted in biological triplicate ($n = 3$) in each condition. Error bars indicate SD. ***$P = 0.0006$, ****$P < 0.0001$ unpaired two-tailed *t*-test compared SFA2*atp20*Δ and SFA2*mic60*Δ against SFA1*atp20*Δ and SFA1*mic60*Δ, respectively. (Right) Respiration rates in *atp20*Δ and SFA2*atp20*Δ cells measured in biological triplicate ($n = 3$) using a Clark electrode. Error bars represent SD. ***$P < 0.0005$, unpaired two-tailed t-test compared against *atp20*Δ.

C SFA2/3 mitochondria do not show defects in ETC complexes or SC formation. BN-PAGE on digitonin-solubilized isolated mitochondria from SFA strains and *atp20*Δ revealed no changes in ETC complex levels (left) or supercomplexes (top right). Mitochondria from *atp20*Δ cells show defects in formation of Complex IV-containing supercomplexes.

D Increasing lipid saturation does not change the status of non-ATP synthase cristae-shaping proteins. To determine the presence of Mgm1p and Mic60p in SFA strains, 10 μg of isolated mitochondria was loaded and subjected to immunoblotting against anti-Mgm1p (C-term) and anti-Mic60p antibodies, respectively.

E Both SFA3 and *atp20*Δ cells showed increased abundance of mtDNA nucleoids compared to WT. Nucleoids were visualized after staining with SYBR Green I (SGI), and the number of nucleoids per cell ($N = 50$ cells) were quantified. Error bars indicate SD. Scale bars, 1 μm. ****$P < 0.0001$, **$P = 0.0020$, unpaired two-tailed t-test against WT for *atp20*Δ and SFA3, respectively.

F SFA3 and *atp20*Δ cells showed increased ER-mitochondria contact distances as analyzed by thin-section TEM. In each condition, the ER-mitochondria distances were measured using IMOD 3D software. Error bars represent SD. $N = 15$ micrographs were quantified for each condition.

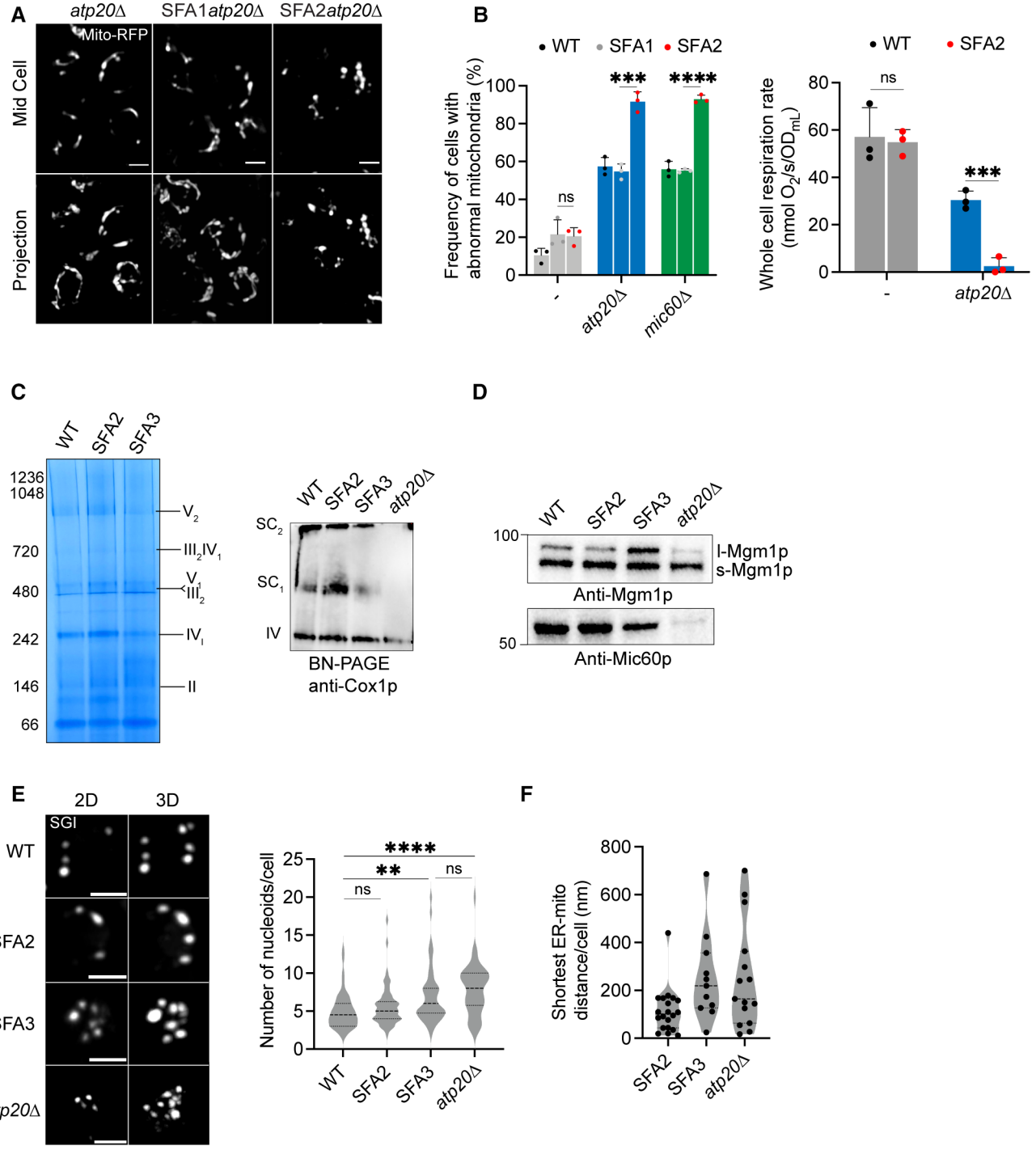
A
atp20Δ
SFA1atp20Δ
SFA2atp20Δ
Mito-RFP
Mid Cell
Projection
B
WT
SFA1
SFA2
Frequency of cells with abnormal mitochondria (%)
ns
***
****
-
atp20Δ
mic60Δ
Whole cell respiration rate (nmol O2/s/ODmL)
ns
***
-
atp20Δ
C
WT
SFA2
SFA3
1236
1048
720
480
242
146
66
V2
III2IV1
V1III2
IV1
II
atp20Δ
SC2
SC1
IV
BN-PAGE
anti-Cox1p
D
100
l-Mgm1p
s-Mgm1p
Anti-Mgm1p
50
Anti-Mic60p
E
2D
3D
SGI
WT
SFA2
SFA3
atp20Δ
Number of nucleoids/cell
****
**
ns
ns
F
Shortest ER-mito distance/cell (nm)

Figure EV1.

Figure EV2. Coarse-grained molecular dynamics predicts an important role for CL in shaping membrane mechanical properties.

A Ideal systems contained lipid compositions of fixed abundance, while changing the unsaturation of the acyl chains from di-unsaturated to monounsaturated. In contrast, the "complex" systems mimicking the mitochondrial lipidomes of SFA strains accounted for headgroup adaptations to increasing saturation, such as increasing PE. Full compositions are listed in Appendix Table S2.

B Example spectral analysis of thermal undulations, used to calculate bending moduli, and lateral pressure profiles, used to calculate spontaneous curvature.

C Chemical structures of CL in dianion (CL-2) and monoanion (CL-1) ionization states.

D In ideal systems, the changing of ionization state of CL from -1 to -2 causes a minor increase in membrane stiffness and a major reduction in spontaneous curvature. Absence of CL increases membrane stiffness and reduces spontaneous curvature as determined through Martini CG-MD. Error bars indicate SD. Error values were derived from one continuous simulation by quantification of statistical inefficiency or analysis of non-overlapping blocks, as described in the Appendix.

E Accounting for headgroup adaptations in complex systems, simulations still show the same trend with dianionic CL and loss of CL showing increases in membrane stiffness and a reduction in spontaneous curvature. Error bars indicate SD. Error values were derived from one continuous simulation by quantification of statistical inefficiency or analysis of non-overlapping blocks, as described in the Appendix.

F While increasing lipid saturation has a minimal effect on membrane stiffness in the absence of CL, the increase in the magnitude of spontaneous curvature suggests that the presence of PE can partially, but not completely, compensate for loss of curvature provided by CL. Error bars indicate SD. Error values were derived from one continuous simulation by quantification of statistical inefficiency or analysis of non-overlapping blocks, as described in the Appendix.

G Modeling of outer leaflet enrichment of CL in the yeast IMM. Simulated changes in CL concentrations previously reported (Gallet *et al*, 1997) results in membrane softening and increased spontaneous curvature. Two sets of simulations were set up with the estimated compositions of the outer and inner IMM leaflets shown in the pie charts. The simulated outer membrane systems were softer (lower stiffness) and had a larger negative spontaneous curvature. The difference in the outer and inner leaflet curvatures was 0.1 ± 0.04 nm^{-1}, which is an estimation for asymmetry-induced c_0. Error bars indicate SD. Error values were derived from one continuous simulation by quantification of statistical inefficiency or analysis of non-overlapping blocks, as described in the Appendix.

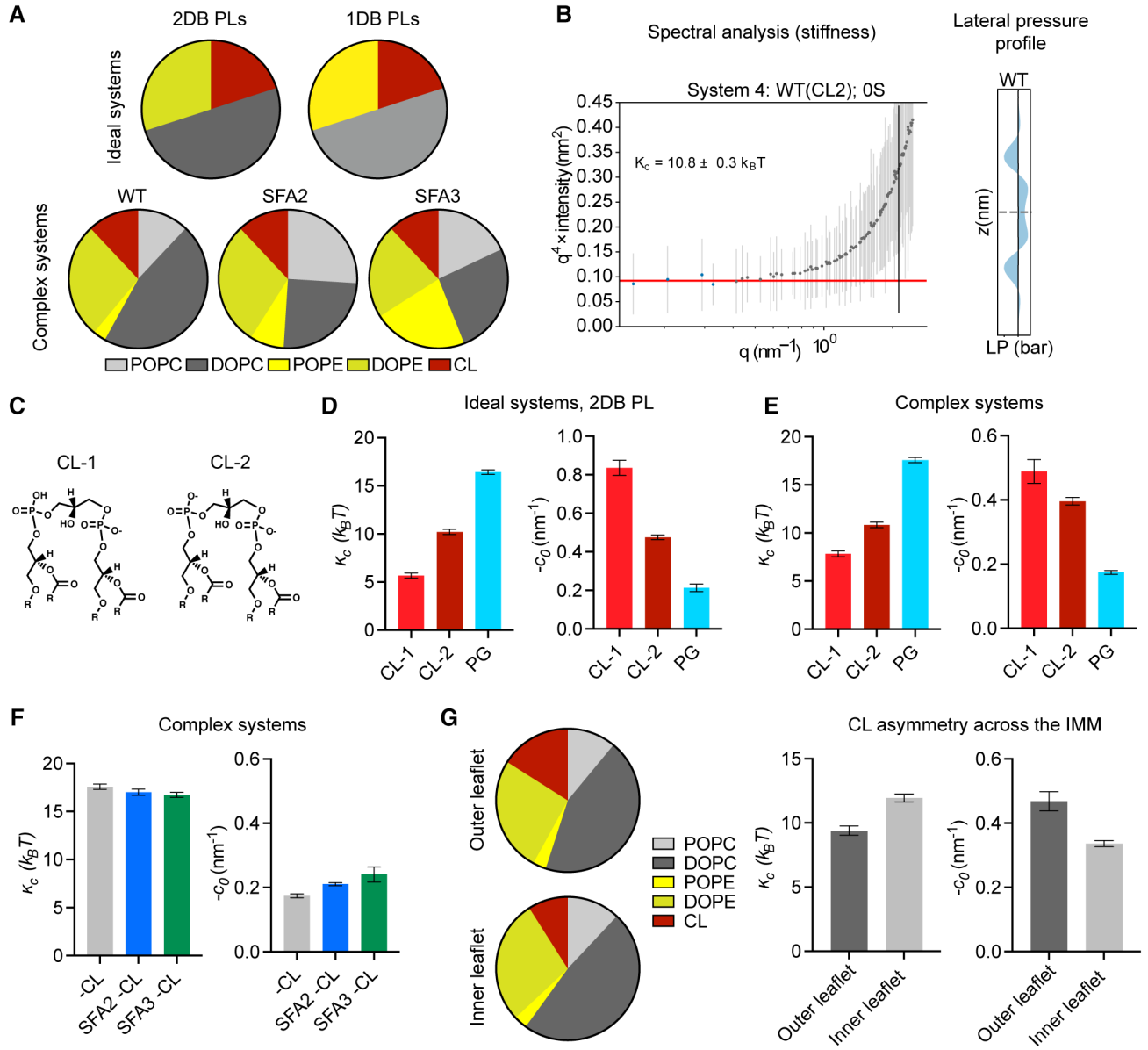

Figure EV2.

Figure EV3. Interactions between cardiolipin synthase, lipid saturation, and ATP synthase dimerization.

A Mitochondrial PL saturation, respiration rate, and mitochondrial abnormality measurements of *CRD1* and *crd1*Δ cells. PL saturation was computed from lipidomics analysis on isolated mitochondria. Respiration measurements were performed using Clark electrode, and mitochondrial abnormalities were determined using confocal microscopy with yeast expressing a matrix-localized mts-RFP ($N > 50$ cells quantified per replicate). Measurements were taken from biological replicates ($n = 3$), error bars indicate SD. An unpaired *t*-test was performed as the statistical test.

B Airyscan confocal micrographs depicting the mitochondrial morphology of aerobic wild-type and *crd1*Δ-expressing IMM protein Cox4-GFP. Scale bars, 2 μm.

C Representative Airyscan confocal micrographs of SFA2*crd1*Δ yeast, grown in the presence and absence of OA, expressing mts-RFP. Scale bars, 2 μm. $^{**}P < 0.005$, unpaired two-tailed *t*-test compared against SFA2*crd1*Δ. Respiration rates of SFA2*crd1*Δ cells in the presence and absence of OA were measured in biological replicates ($n = 3$) using a Clark electrode. Error bars indicate SD. $^{*}P < 0.05$ unpaired two-tailed *t*-test.

D Loss of CL and ATP synthase dimerization results in complete ablation of mitochondrial morphology and structure as assayed by analysis with mts-RFP. $N > 50$ cells were counted in biological triplicate ($n = 3$) in each condition. Error bars indicate SD. Individual deletion of Crd1p results in normal mitochondrial morphology, while half of the cells in *atp20*Δ still retain normal morphology. Scale bars, 2 μm.

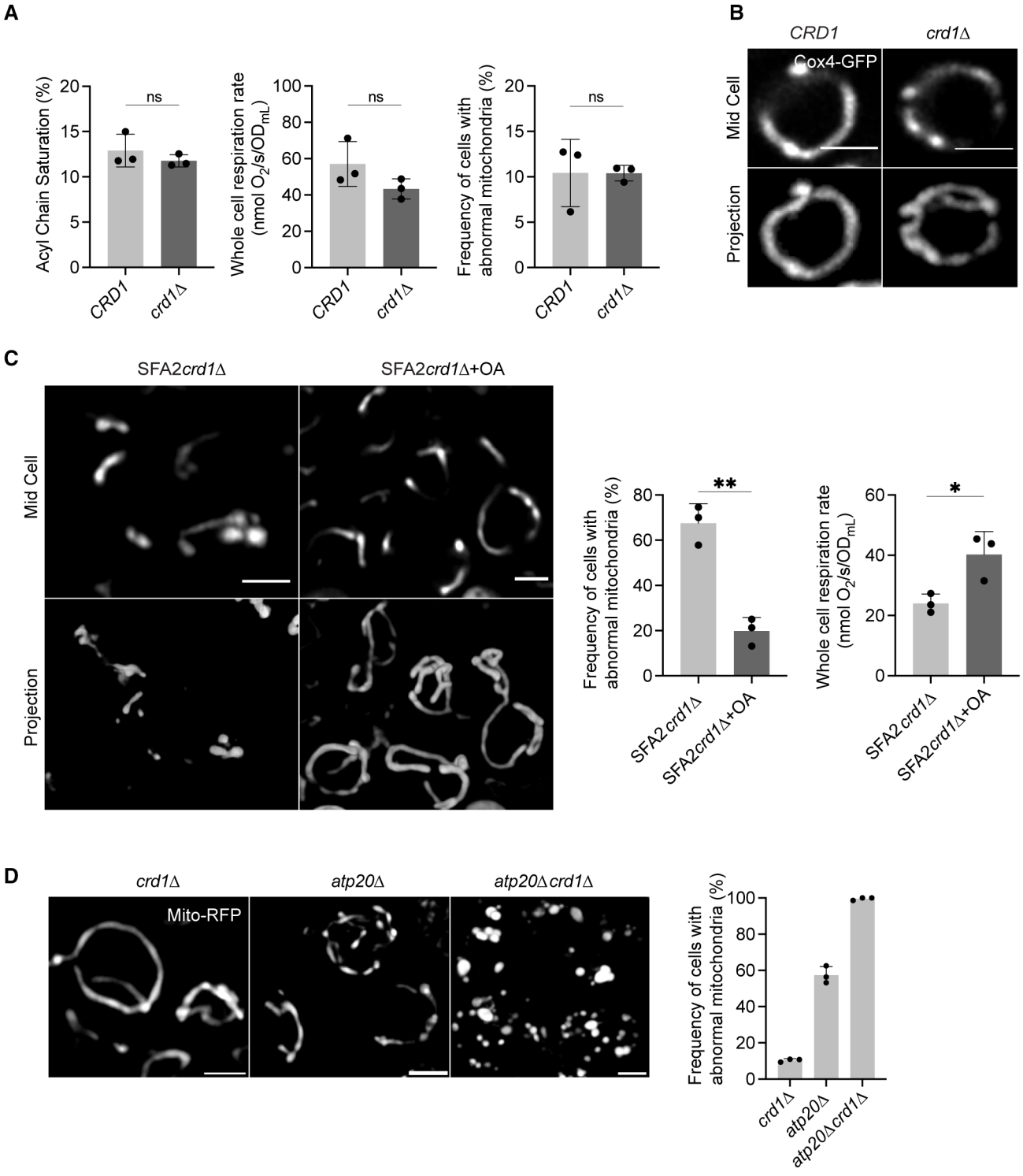

Figure EV3.

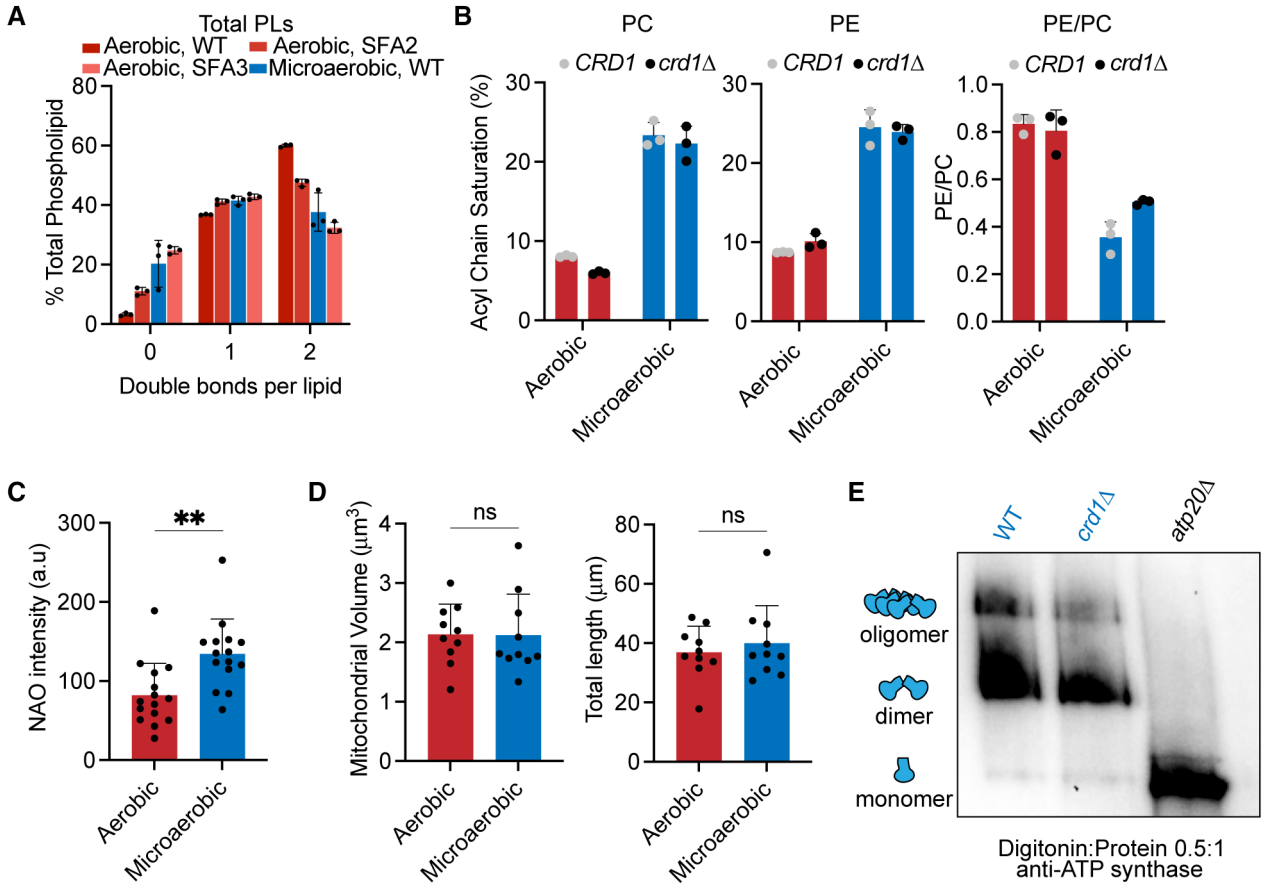

Figure EV4. Microaerobic cells exhibit an intermediate level of lipid saturation between SFA2/3 and retain mitochondrial volume and ATP synthase dimers.

A Lipidomic analysis of the double bond distribution of microaerobic yeast ($n = 3$ biological replicates) shows decreased di-unsaturated PL chains and increased saturated PL chains. This is consistent with an intermediary increase in PL saturation between SFA2 and SFA3 levels. Error bars indicate SD.

B The major cellular PL classes, PC and PE, show increased lipid saturation under microaerobic conditions ($n = 3$ biological replicates). Also shown is the decrease in whole-cell PE/PC ratio under microaerobic conditions, as observed in SFA strains (Fig 3D). Error bars indicate SD.

C CL content in microaerobic vs. aerobic conditions assayed by staining with 100 nM nonyl acridine orange (NAO). NAO intensities were quantified by line profile analysis from confocal micrographs of $N > 15$ cells in each condition. $^{**}P = 0.0021$ unpaired two-tailed t-test against WT. Error bars indicate SD.

D Microaerobic growth conditions do not induce changes to mitochondrial volume or length. Mitograph software was used to measure the voxel volume and total length of mitochondrial tubules from confocal images taken from yeast cells grown in microaerobic vs. aerobic conditions. $N = 10$ cells were quantified from each condition. Error bars indicate SD. An unpaired t-test was performed as the statistical test.

E Microaerobic cells still contain ATP synthase dimers. Digitonin-solubilized crude mitochondria from microaerobic cultures were separated by BN-PAGE and immunoblotted with anti-ATP synthase antibodies. Crude mitochondria from microaerobic *atp20*Δ was used as a monomeric control.

Figure EV5. Epistasis between lipid saturation and cardiolipin metabolism in HEK293 cells.

A Knockdown of *CRLS1* by siRNA (siCRLS1) results in a ~ 50% decrease in CRLS1 intensity as normalized to β-Actin intensity compared to the scrambled control (siSCR). Error bars indicate SD from $n = 2$ independent transfections.

B Coordinated increase in saturated fatty acid and depletion of CL result in decreased oxygen consumption rate (OCR) and extracellular acidification rate (ECAR). OCR and ECAR were measured from 10,000 cells in triplicates ($n = 3$) in each condition assayed using Seahorse respirometry. Cells treated with both mild concentrations (50 μM) of PA and siCRLS1 showed a quiescent metabolic phenotype.

C Knockdown of *CRLS1* results in loss of tubular mitochondrial morphology upon treatment with 50 μM PA. Representative images of single cells transfected with scrambled (siSCR) or *CRLS1* (siCRLS1) siRNAs and subsequently treated with BSA or BSA complexed with 50 μM PA. Cells were stained with Mitotracker DeepRed. Images show individual cells. Scale bars, 5 μm.

D *CRLS1* knockdown cells treated with 50 μM PA are bereft of abundant cristae sheets observed in control cells or those treated with only siCRLS1 or 50 μM PA. Representative TEMs of individual mitochondria are shown from each condition. Scale bars, 500 nm.

E *CRLS1* knockdown cells treated with 50 μM PA show decreased cristae density and cristae length. Cristae density was quantified as the number of cristae per mitochondrial area and assessed from $N = 35$ mitochondria. ****$P < 0.0001$ unpaired *t*-test of siCRLS1 with 50 μM PA against siSCR with 50 μM PA, *$P < 0.025$ unpaired *t*-test of siCRLS1 with 50 μM PA against siSCR and siCRLS1. Cristae length was measured in $N = 100$ cristae in each condition. ****$P < 0.0001$ unpaired t-test of siCRLS1 with 50 μM PA against siSCR with 50 μM PA and siCRLS1. Error bars indicate SD.

F Knockdown of *CRLS1* does not change the acyl chain saturation in aerobic or microaerobically grown cells, but the latter feature higher lipid saturation due to reduced oxygenation. Error bars indicate SD. Samples were analyzed in biological triplicates ($n = 3$). An unpaired *t*-test was performed as the statistical test.

G Under 1% oxygen growth conditions, knockdown of *CRLS1* results in loss of tubular mitochondrial morphology. Cells were incubated in microaerobic chambers for 72 h or normoxic chambers for 48 h prior to staining with Mitotracker DeepRed. Images show individual cells. Scale bars, 5 μm.

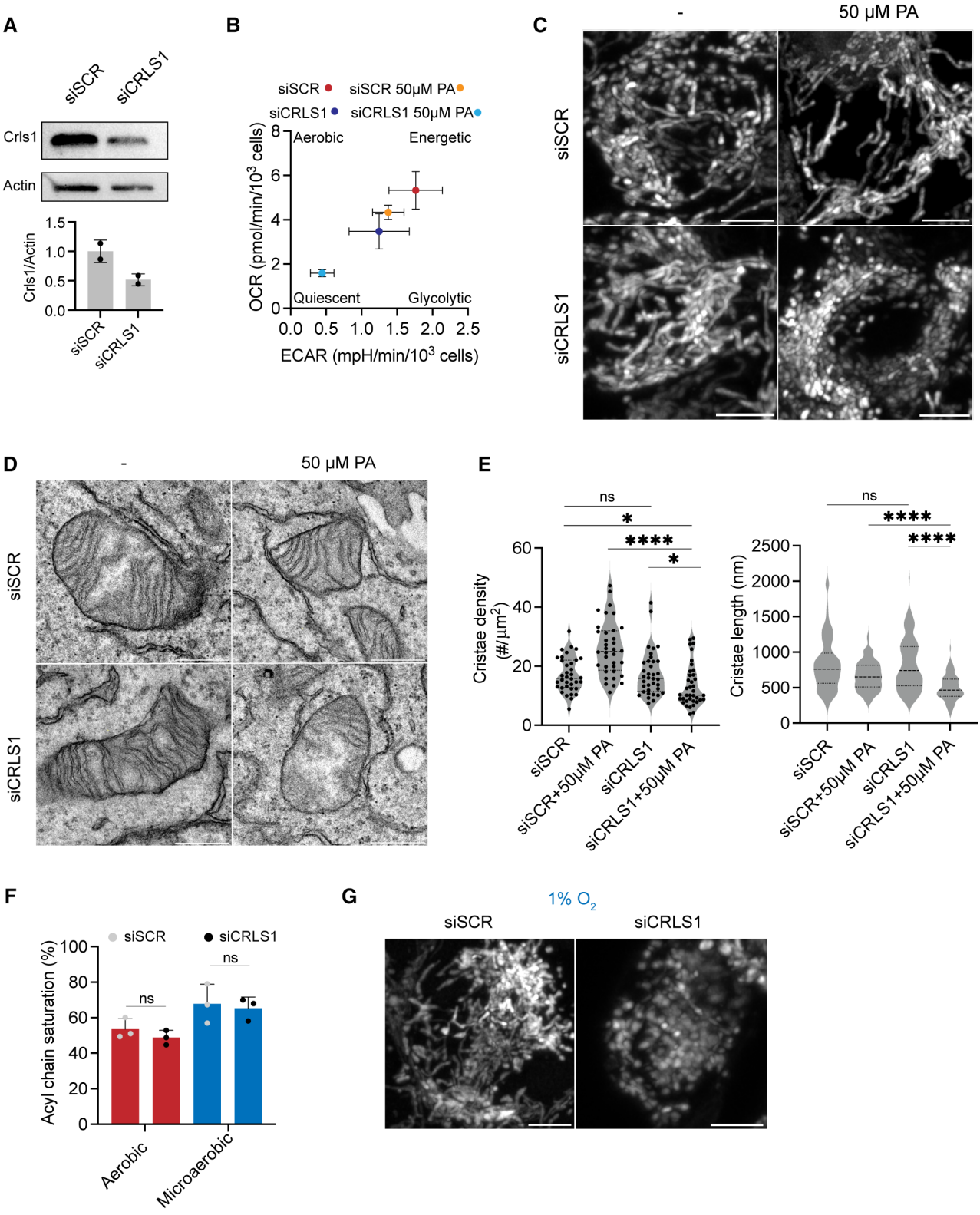
A
siSCR
siCRLS1
Crls1
Actin
Crls1/Actin
1.5
1.0
0.5
0.0
siSCR
siCRLS1
B
siSCR
siSCR 50μM PA
siCRLS1
siCRLS1 50μM PA
Aerobic
Energetic
Quiescent
Glycolytic
OCR (pmol/min/10^3 cells)
ECAR (mpH/min/10^3 cells)
C
-
50 μM PA
siSCR
siCRLS1
D
-
50 μM PA
siSCR
siCRLS1
E
ns
*
****
*
Cristae density (#/μm^2)
Cristae length (nm)
siSCR
siSCR+50μM PA
siCRLS1
siCRLS1+50μM PA
F
siSCR
siCRLS1
ns
ns
Acyl chain saturation (%)
Aerobic
Microaerobic
G
1% O2
siSCR
siCRLS1

Figure EV5.